Applied Clay Science 245 (2023) 107139

Contents lists available at ScienceDirect

Applied Clay Science

journal homepage: www.elsevier.com/locate/clay

Research Paper

Efficacy of functionalized sodium-montmorillonite in mitigating alkali-silica reaction

Dayou Luo, Jianqiang Wei *

Department of Civil and Environmental Engineering, Francis College of Engineering, University of Massachusetts Lowell, Lowell, MA 01854, USA

ARTICLE INFO

Keywords:
Montmorillonite
Functionalization
Alkali-silica reaction
Expansion
Mechanism analysis
Microstructure

ABSTRACT

Alkali-silica reaction (ASR) is a fatal deterioration that can cause volume expansion, cracking, and premature failure of concrete. In this study, the efficacy of sodium montmorillonite (NaMt) organically functionalized with two non-ionic surfactants (ONaMts) in mitigating ASR is investigated by determining the expansion and cracking behavior of mortars containing reactive aggregates. The underlying mitigation mechanisms were analyzed through the quantification of reaction products and in-situ characterizations of ASR gels. The results revealed that, compared with raw NaMt, ASR-induced expansion and cracking can be more substantially mitigated in the presence of ONaMts, which is supported by the improved consumption of portlandite and reduced formations of both crystalline and amorphous ASR gels. The functionalized ONaMts appeared to further suppress the formation of Q^3 polymerization sites, decrease the [K + Na]/Si atomic ratio and increase the Al/Ca in ASR gels.

1. Introduction

Alkali-silica reaction (ASR), commonly known as “concrete cancer”, is one of the main deterioration mechanisms to induce durability problems in concrete structures. It was widely reported that ASR is a harmful reaction occurring between the alkali species (such as Na^+, K^+, OH^-) present in cement and the silica dissolved from reactive aggregates (Kim et al., 2015; Luo et al., 2022). This reaction leads to the formation of ASR gels, which can absorb moisture and swell to cause cracks in both aggregate and cement paste resulting in damages and further deteriorations in concrete structures (Rajabipour et al., 2015; Wei et al., 2019).

The detrimental effect of ASR in concrete structures has driven extensive investigations in ASR mitigation approaches over the past decades, which can be categorized into three main strategies: 1) eliminating the reactants of ASR in raw materials by using non-reactive aggregates or low-alkali cement (Carles-Gibergues et al., 2008); 2) incorporating supplementary cementitious materials (SCMs), such as fly ash (Saha et al., 2018), metakaolin (Luo et al., 2022), montmorillonite (Wei et al., 2019), etc.; 3) adding chemical admixtures, such as lithium salts (Collins et al., 2004), calcium nitrate (Oey et al., 2020), or others. Although promising results have been documented, the shortcomings of these conventional approaches have also been reported. First, non-reactive aggregates are not readily available in many regions, where the use of low-alkali cement alone may not be sufficient (Rajabipour et al., 2015). Second, the scarcity and high cost of lithium salts raise questions about their feasibility in the construction industry. Furthermore, the negative influence of lithium admixtures on early-age hydration and shrinkage behavior of cement has been reported (Millard and Kurtis, 2008). When using SCMs, a high cement substitution level is required to sufficiently mitigate ASR, while this can result in compromised mechanical strength of the concrete (Trümer et al., 2019). Additionally, the decreasing availability of fly ash (roughly 60% reduction in the last decade) due to the retirement of coal-based plants (Kaladharan et al., 2019) highlights the urgency to utilize naturally abundant alternatives.

Montmorillonite (Mt) is a clay mineral belonging to the smectite group and can be commonly obtained in bentonite deposits. This widely abundant mineral possesses a three-layered structure composed of two silica tetrahedral layers sandwiching an alumina octahedral layer (Li et al., 2023). The interlayer space of Mt. is typically occupied by exchangeable cations, i.e., sodium, calcium, or magnesium, corresponding to sodium Mt. (NaMts), calcium Mt., or magnesium Mt., respectively. Mt. nanoclay particles, known for their high pozzolanic reactivity due to high amorphous aluminate and silicate contents, have been widely utilized to modify cement hydration and improve concrete

* Corresponding author at: Department of Civil and Environmental Engineering, University of Massachusetts Lowell, 1 University Avenue, Shah Hall 200, Lowell, MA 01854, USA.
E-mail address: Jianqiang_wei@uml.edu (J. Wei).

https://doi.org/10.1016/j.clay.2023.107139
Received 24 June 2023; Received in revised form 8 September 2023; Accepted 9 September 2023
Available online 18 September 2023

performance (Calabria-Holley et al., 2017; Chang et al., 2007; Papatzani, 2016; Wei and Gencturk, 2019). However, due to its high water absorption and poor dispersion within the cement matrix, Mt. can only replace 1% to 3% cement to avoid compromising concrete properties (Mesboua et al., 2018). A recent study conducted by the authors (Luo and Wei, 2022a) demonstrated that both the dispersion and pozzolanic reactivity of NaMt in the cement matrix can be substantially enhanced after non-ionic functionalization. Furthermore, the hydration and compressive strength of cement were found to be improved along with decreased autogenous shrinkage and densified microstructure by incorporating organically functionalized NaMt (ONaMt) (Luo and Wei, 2022b, 2023).

In light of the enhanced role of ONaMts over NaMt in cement modification, the feasibility of utilizing ONaMts as a novel approach to suppress ASR is explored in this study by evaluating the mitigation of volume expansion and cracking behavior in mortars containing reactive aggregates. The underlying mitigation mechanisms were investigated by analyzing the formation of reaction products in the mortar matrix and via in-situ characterizations of ASR gels, including thermogravimetric analysis (TGA), X-ray diffraction analysis (XRD), attenuated total reflectance-Fourier transform infrared (ATR-FTIR), Raman spectroscopy, and field emission scanning electron microscopy (FE-SEM) combined with energy dispersive X-ray analysis (EDS). To the best of our knowledge, no such approach has been reported and the findings presented in this study are expected to provide a better understanding of the nanoengineered clay-modified cement in designing durable concrete.

2. Materials and methods

2.1. Materials

Type I/II ordinary Portland cement (Quikrete) and NaMt (Sigma-Aldrich) were used as cementitious materials in this study. Table 1 summarizes the chemical and mineralogical compositions of these materials determined via X-ray fluorescence (XRF) and Bogue calculation. It is observed that the silicate and aluminate phases ($SiO_2 + Al_2O_3$) in NaMt are 79.2%, which is 3.2 times that found in the cement. The NaMt exhibits a Na_2O content of 5.03%. It was reported that the alkalis (especially Na^+) from NaMt could be either exchanged with Ca^+ from the concrete pore solution or released to the concrete pore solution directly due to the collapse of NaMt after dissolution and reaction (Rajabipour et al., 2015). The particle size distributions of cement and NaMt before and after functionalization measured by laser diffraction are shown in Fig. A1 (see Appendix A). The Methylene blue test per ASTMC837, 2019 indicates that the cation exchange capacity (CEC) of the NaMt used in this study is 116.48 meq/100 g. Highly reactive sand sourced from EI Paso, Texas, United States, with a relative density and fineness modulus of 2.39 and 2.96, respectively, was used. As specified in ASTMC1260, 2022, the required grading fraction was achieved by sieving the reactive aggregates: 10% (43.75 mm–2.36 mm), 25% (2.36 mm–1.18 mm), 25% (1.18 mm- 0.6 mm), 25% (0.6 mm- 0.3 mm), and 15% (0.3 mm- 0.15 mm). As characterized in previous studies (Fournier et al., 2009; Kim et al., 2015; Sanchez et al., 2018; Trottier et al., 2021; Wei et al., 2019), the sand is polymictic consisting of granites (potassium feldspar and sodium feldspar), volcanic rock (cristobalite), quartzite, chert, quartz, silicon carbide, and calcium carbonate, while chert that contains readily dissolved silica plays the most role in the reactivity of the sand. Sodium hydroxide with a purity of 97% (Thermo Fisher Scientific) was used for making the 1 N NaOH solution used in the mortar bar test. Two chemically pure non-ionic surfactants, polyoxyethylene (9) nonylphenylether (PONPE9) and *t*-octyl phenoxy poly ethoxyethanol (TX100), purchased from Sigma-Aldrich, were used to organically functionalize NaMt. The average molar mass of PONPE9 and TX100 is 660 g/mol and 647 g/mol, respectively.

2.2. Functionalization of montmorillonite and sample preparation

The NaMt clay particles were organically functionalized by an ion exchange method (Taleb et al., 2018). As shown in Fig. 1, 100 g of NaMt particles were first mixed with the specific amounts (0.2CEC or 0.6CEC) of surfactants (PONPE9 or TX100) in 1 L of deionized (DI) water at 500 rpm and 25 °C for 30 min. The ONaMt was then separated from the suspension via centrifugation at 1400 rpm for 15 min. Then, the centrifuged clays were oven-dried at 70 °C for 24 h, followed by a grinding process with a planetary ball mill at 900 rpm for 2 h to obtain a similar particle size with the raw NaMt (the median particles sizes of 11.3–12.8 μm), and the corresponding particle size distribution was illustrated in Fig. A1 (see Appendix A). More details about the functionalization process and characterization of the ONaMts can be found in the authors' previous studies (Luo and Wei, 2022a, 2023).

The ASR-induced expansion of the mortar bar specimens containing highly reactive sands was monitored for a period of 60 days using an accelerated mortar bar test according to ASTMC1260, 2022. Prismatic mortar bars with a dimension of 25.4 mm × 25.4 mm × 255 mm were cast as per ASTMC1260, 2022 with 2 repetitions per group to measure the ASR-induced expansion. The water-to-binder ratio (w/b) and binder-to-sand ratio were fixed at 0.47 and 2.03, respectively. The proportions of the mortar samples, where six groups in total were prepared, are summarized in Table 2. Plain cement with reactive sands was prepared as the control group (PC), and a 3 wt% replacement of cement with raw NaMt, named NaMt, was cast to examine the ASR mitigation effect of the NaMt clay particles. Four groups containing 3 wt% of 0.2P-NaMt, 0.2 T-NaMt, 0.6P-NaMt, and 0.6 T-NaMt were cast for investigating the efficiency of the ONaMts on ASR mitigation, in which P and T represent the surfactants PONPE9 and TX100, respectively, while the numbers before P and T indicate the dosage of surfactants used to functionalize NaMt. For instance, 0.2P-NaMt represents the NaMt functionalized by PONPE9 at 0.2 of its CEC. To prepare the mortar bars, the cement, dry clay particles (NaMt or ONaMt), and reactive sands were first mixed in a mechanical mortar mixer for 1 min. Then, the mixing water was added into the mixer followed by a 2-min mixing at a low-speed of 60 rpm. After a 1-min rest, a 3-min of high-speed mixing at 120 rpm was performed until homogeneously mixed mortars were obtained. After one day of casting, the mortar bars were demolded and immersed in tap water at 23 °C in a sealed container, which was then conditioned at 80 °C in a mechanical oven for 24 h.

2.3. Test specifications

Following ASTMC1260, 2022, the mortar bars were transferred to 1 N NaOH solution at 80 °C after 48 h of casting. The initial length of the mortar bars at the beginning of this hot-alkali treatment was recorded as

Table 1
Chemical and mineralogical compositions of cement and NaMt (wt%).

	CaO	SiO_2	Al_2O_3	SO_3	Fe_2O_3	MgO	Na_2O_{eq}		C_3S	C_2S	C_3A	C_4AF	LS
Cement	62.7	20.1	4.8	3.5	3.2	3.4	0.6		54	17	7	10	1.2
NaMt	0.949	62.0	17.2	0.199	6.51	7.35	K_2O 0.072	Na_2O 5.03	TiO_2 0.224	ZnO 0.0283	ZrO_2 0.146	Cl 0.185	Compton 0.86

Note: Na_2O_{eq}: Equivalent alkali ($Na_2O + 0.658K_2O$); C_3S: tricalcium silicate; C_2S: dicalcium silicate; C_3A: tricalcium aluminate; C_4AF: tetra-calcium aluminoferrite; LS: Limestone; $CaCO_3$ in LS: 92.0%.

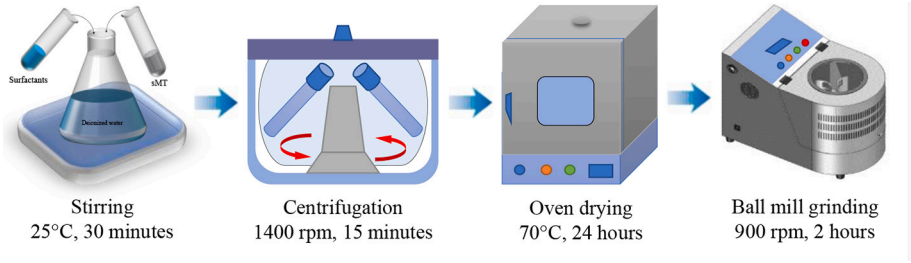

Fig. 1. Schematic diagram for the non-ionic functionalization process.

Table 2
Amounts of materials for mortar bar test.

ID	Cement (g)	NaMt (g)	Water (g)	Sand (g)
PC	440.0	–	206.8	893
NaMt	426.8	13.2	206.8	893
0.2P-NaMt	426.8	13.2	206.8	893
0.6P-NaMt	426.8	13.2	206.8	893
0.2T-NaMt	426.8	13.2	206.8	893
0.6T-NaMt	426.8	13.2	206.8	893

a zero reading. The subsequent length change of the mortar bars was measured using a digital comparator after 12 and 24 h, followed by once per day during the first week, and two readings per week until the completion of the 60-day period. After 60 days of immersion, the mortar bars were dried with paper towels and the surface cracking behavior was assessed by a digital microscope. At the end of the expansion test, the average crack width on selected surface of the mortars was determined based on at least 10 measurements for each mortar bar (20 measurements for each group) using ImageJ.

After 60 days of immersion (62 days from casting), TGA, XRD, and ATR-FTIR were conducted on ground powders (passing through a 40 μm sieve) of the mortar bars. Prior to the analysis, the powders were vacuum dried for 20 min. TGA was performed using a Perkin Elmer TGA 4000 thermogravimetric analyzer. Approximately, 20 mg of powder sample was added into an alumina sample pan, which was then placed on the micro-balance and heated in the furnace chamber. The sample was kept at 30 °C for 1 min for equilibrium and then heated to 800 °C at a heating rate of 15 °C/min. To provide an inert atmosphere, pure N_2 gas was used at a constant flow rate of 20 mL/min. The contents of calcium hydroxide (CH) (mass fraction) were determined from the weight loss between 400 °C and 510 °C (w(CH_1) in Eq. (1)) and the one converted from calcium carbonate (CC) between 590 °C and 770 °C (w(CC) in Eq. (2)), which is mainly due to the carbonation of CH during sample preparation (w(CH_2) in Eq. (3)) (Luo and Wei, 2022b). Therefore, the CH contents were determined by summing CH_1 and CH_2 (Eq. (4)):

$$w(CH_1) = \left[\frac{W_{400}-W_{510}}{W_{510}}\right] \times \frac{M_{CH}}{M_{H_2O}} = \left[\frac{W_{400}-W_{510}}{W_{510}}\right] \times 4.1 \times 100\% \quad (1)$$

$$w(CC) = \left[\frac{W_{590}-W_{770}}{W_{770}}\right] \times \frac{M_{CC}}{M_{CO_2}} = \left[\frac{W_{590}-W_{770}}{W_{770}}\right] \times 2.27 \times 100\% \quad (2)$$

$$w(CH_2) = w(CC) \times \frac{M_{CH}}{M_{CC}} = w(CC) \times 0.74 \quad (3)$$

$$w(CH) = w(CH_1) + w(CH_2) \quad (4)$$

where, W_n is the mass at temperature n °C. The temperature ranges were determined on the TGA and DTG curves via a tangent method (Kim and Olek, 2012). M_{CH}, M_{H2O}, M_{CC}, and M_{CO2} are the molar mass of CH, H_2O, CC, and CO_2, respectively.

A Proto AXRD powder X-ray diffractometer equipped with a CuKα source (λ =1.54 Å) was used for XRD analysis. The same ground powder samples of mortars as used in TGA (passing through a 40 μm sieve) were scanned from 15° to 65° (2θ) in a stepwise mode with a step size of 0.02° (2θ). The XRD scanning was conducted at 30 kV and 20 mA with a total scanning time of 42 min. The obtained XRD patterns were analyzed using XRDWIN®PD software combined with the Crystallography Open Database (COD) (Gražulis et al., 2009). The crystalline phases identified from the XRD data were quantified by XRD-Rietveld refinement using the built-in Whole-Pattern Fitting in XRDWIN®PD. The amorphous contents were excluded from the calculation by a 7th-order of Chebyshev polynomial background removal. The crystalline peaks were fitted with the Voigt model using a full profile fitting procedure (Le Saoût et al., 2011). The R-factor (also known as the residual factor) is the most straightforward index for a fitting criterion for XRD-Rietveld refinement. A lower R-value is normally considered a better refinement fitting, and a value lower than 0.2 is a desirable target (Morris et al., 1992). The crystallographic index files (CIF) of the minerals discussed in Section 3.2.2 were employed in the Rietveld refinement.

FTIR spectroscopy was carried out using a Thermo Fisher Scientific Nicolet iS10 FTIR spectrometer. Before testing the specimens, the spectrum of the diamond crystal was collected, and the background was automatically subtracted while collecting the data. The ground mortar powders were pressed by the diamond and scanned via attenuated total reflection (ATR) mode. The spectra between 4000 and 400 cm^{-1} were acquired by the co-addition of 128 scans with a canning time of 190 s and a resolution of 4 cm^{-1}.

After 60 days, thin slides were cut from the selected mortar bars (PC, NaMt, 0.6P-NaMt, and 0.6T-NaMt) and vacuum dried. A Horiba LabRam HR Evolution Raman spectrometer-confocal Raman microscope was used to record the Raman spectra on the disk mortars samples by focusing on the hydrated cement pastes, the ASR gels inside the cracks of aggregate, and the ASR gels extruded into the cracks of cement pastes. The Raman spectra were collected with two accumulations in the range of 100 cm^{-1} to 1800 cm^{-1} at a resolution of 0.5 cm^{-1} with a 633 nm excitation laser source and a maximum power of 3.25 mW. The received data was processed with LabSpec 6 Spectroscopy Suite to remove the background and fit the peaks with the Gaussian function.

The microstructure of selected mortars (PC, 0.6P-NaMt, and 0.6T-NaMt) after 60 days of accelerated ASR treatment was investigated on thin disks with a thickness of <2 mm using a JEOL JSM 7401F FE-SEM under an accelerating voltage of 10.0 kV. Before the SEM test, the mortar disks were vacuum dried at 25 °C and then coated with a thin gold layer using a vacuum sputter coater (Denton Vacuum Desk IV). The elemental quantifications of the ASR gels were performed using an EDS Genesis XM2 Imaging System composed of a 10 mm^2 Si (Li) detector with a SUTW window under an accelerating voltage of 15.0 kV. At least 30 points were collected from the specific type (crystalline and amorphous) of ASR gels for each group.

3. Results and discussion

3.1. ASR expansion

3.1.1. ASR expansion

Fig. 2a shows the ASR-induced expansion behavior of the mortar bars with and without 3% cement replacement with NaMt/ONaMts for a period of up to 60 days. The control group (PC) yielded an expansion of 0.97% after 14 days, which is higher than the indication (> 0.2%) of potential for deleterious ASR as defined in ASTMC1260, 2022, indicating the extremely high reactivity of the sand used in the current study. After 60 days, the ASR-induced expansion of PC increased to 1.42%. By replacing 3 wt% cement with NaMt, the 14-day and 60-day ASR expansions were decreased to 0.80% and 1.21%, respectively, which are 0.17% and 0.21% lower than that of PC. In the presence of the functionalized ONaMts, both the ASR expansion and expansion rate of the mortar bars were further decreased. 0.2P-NaMt and 0.6P-NaMt showed 14-day expansions of 0.64% and 0.61%, respectively, which are 0.33% and 0.36% lower than that of PC, and 0.16% and 0.19% lower than that of NaMt. The superior efficiency of ONaMts functionalized with PONPE9 over that with TX100, at both dosages (0.2CEC and 0.6CEC), in mitigating ASR was observed. This is especially the case for the early-age ASR suppression indicated by the 0.03% lower 14-day expansion.

Lower expansion rates were also obtained in the ONaMts groups than that of PC and NaMt. The maximum expansion rate of 0.147%/day was yielded by PC at 2 days, as seen in Fig. 2b. The incorporation of NaMt resulted in a 0.22% lower maximum expansion rate. The maximum expansion rate among these ONaMts groups was reached by 0.2T-NaMt after 2 days of immersion with a value of 0.131%/day, which is 10.9% and 10.8% lower than that of PC and NaMt, respectively. On the other hand, 0.6P-NaMt presented the lowest expansion rate of 0.117%/day at 2 days of immersion, which is 20.4% and 10.7% lower than that of PC and 0.2T-NaMt, respectively.

3.1.2. Cracking behavior

As shown in Fig. 3a, after being immersed in 1 N NaOH at 80 °C for 60 days, the PC group showed clear cracks on its surface, while the mortar bars containing 3 wt% raw NaMt exhibited fewer cracks with smaller size, indicating the suppressed ASR. When replacing cement with 3 wt% 0.2P-NaMt or 0.2T-NaMt, the cracks formed in the mortars exhibited further decreases. Indicated by the microcracks that can only be detected under a microscope, the 0.6P-NaMt and 0.6T-NaMt presented more effective roles in mitigating ASR than NaMt, 0.2P-NaMt, and 0.2T-NaMt. As shown in Fig. 3b, a linearly positive correlation between the ASR expansion and the average crack width was observed from the investigated groups. The control group yielded the highest average crack width of 0.44 mm. In the presence of NaMt, an 18.2% lower average crack width was obtained. In line with the suppression of ASR expansion, more pronounced crack width decreases were observed from the groups containing ONaMts. 0.2P-NaMt and 0.2T-NaMt presented average crack widths of 0.18 mm and 0.21 mm, which are 59.1% and 52.3% lower than that of PC, and 50.0% and 41.7% lower than that of NaMt, respectively. By increasing the dosages of the surfactants in NaMt, the average crack width further decreased in 0.6P-NaMt and 0.6T-NaMt, which are 70.4% and 63.6% lower than that of PC, respectively. The enhanced role of ONaMts in mitigating ASR-induced expansion and cracking might be due to the improved dispersion and pozzolanic reactivity of NaMt after the functionalization as demonstrated in (Luo and Wei, 2022a), while additional analyses are needed to fully uncover the underlying mechanisms (see Section 3.2 below).

3.2. Mechanism analysis

3.2.1. Thermogravimetric analysis

Fig. 4a and b show the TGA and DTG curves for mortars with and without 3 wt% cement replacement with NaMt/ONaMts after 60 days of exposure to 1 N NaOH and 80 °C, respectively. Four main mass drop ranges from Fig. 4a and the corresponding DTG peaks shown in Fig. 4b can be observed. The initial weight loss between 30 °C and 260 °C is due to the evaporation of free water and weekly bound water in C-S-H, while the former mainly occurs below 105 °C and the latter occurs between 105 °C and 260 °C (Morandeau et al., 2014). It is worth noting that these two weight losses occurred closely and resulted in an overlapped DTG peak in Fig. 4b. Interestingly, for the specimens containing NaMt or ONaMts, this peak shifted to a higher temperature of around 140 °C, which might be due to the decrease of free water contents in these specimens and the increases in C-S-H due to the pozzolanic reactions. Due to its unstable nature under the curing condition (i.e., 1 N NaOH and 80 °C), no significant weight loss of ettringite was observed. The weight loss between 300 °C to 420 °C is due to the decomposition of hydrotalcite. However, no significant change in the hydrotalcite peak was found from these groups, which might be due to the limited magnesium resources in the systems.

The third and fourth weight losses detected in the vicinities of 450 °C and 650 °C are due to the dehydroxylation of CH and decarbonization of

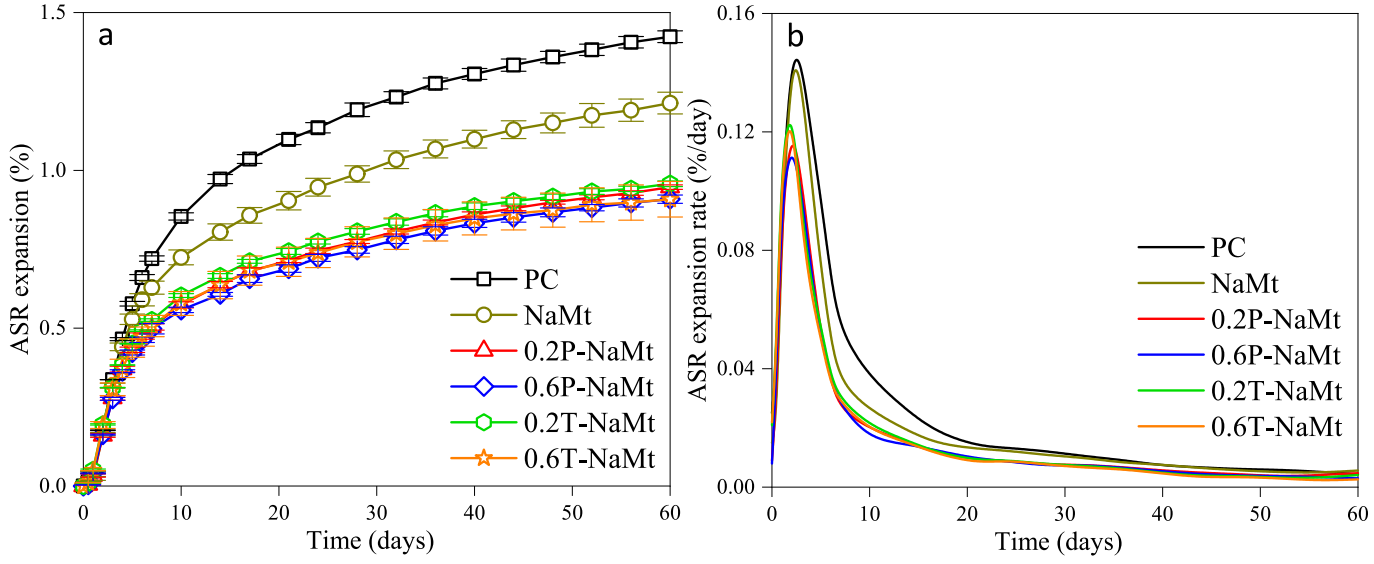

Fig. 2. (a) ASR expansion and (b) expansion rate of the mortar bars.

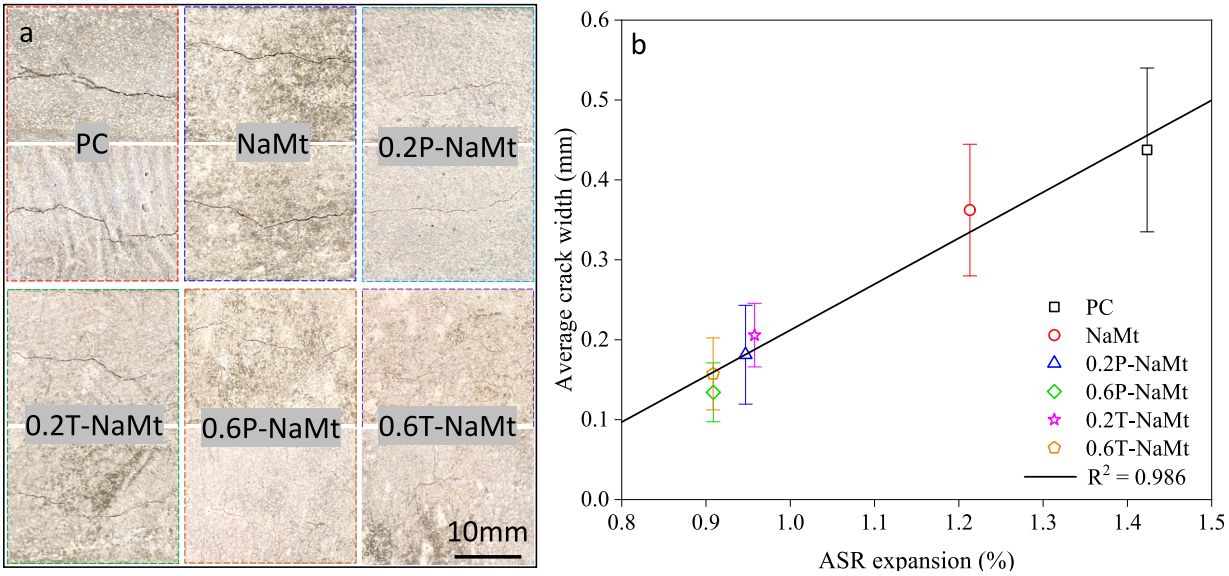

Fig. 3. (a) Surface cracks of the mortar bars immersed in 1 N NaOH solution at 80 °C for 60 days and (b) the correlation between ASR expansion and the average crack width.

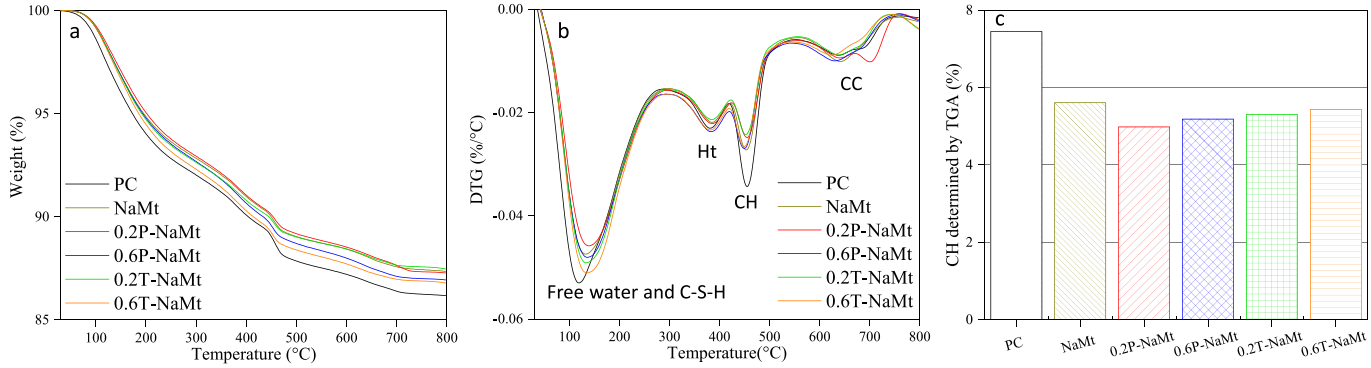

Fig. 4. (a) TGA and (b) DTG curves of mortar powders after 60 days of treatment, and (c) CH contents. Ht: hydrotalcite; CH: portlandite; CC: calcite.

CC, respectively. By taking these two decompositions into account (Eq. (4)), the CH contents (mass fraction) were determined and shown in Fig. 4c. It should be noted that CH is one of the main products from cement hydration, but it can be consumed by the incorporated NaMt/ONaMt via pozzolanic reaction to form additional C-S-H (Wu et al., 2022), which attributes to the higher C-S-H peaks from the NaMt/ONaMt groups than that of PC in the DTG curves presented in Fig. 4b. As seen in Fig. 4c, around 7.5% of CH was precipitated in PC, while it decreased to 5.6% in the NaMt group, which might be due to the pozzolanic reaction between NaMt and CH. It is interesting to see that a further decrease of CH was found in the groups containing ONaMts, showing the CH contents in the range of 5.0% to 5.4%. 0.2P-NaMt showed the lowest CH content of 5.0%, which is 2.5% and 0.6% lower than that in PC and NaMt, respectively. This is consistent with the observations in the authors' previous studies (Luo and Wei, 2022a, 2022b) that 0.2P-NaMt showed the highest pozzolanic reactivity among all these ONaMts. It is noteworthy that, although 0.6P-NaMt and 0.6T-NaMt showed higher CH than that of 0.2P-NaMt and 0.2T-NaMt, lower ASR expansions were observed from these two high-surfactant loading groups. This mismatching indicates that CH consumption is not the sole reason for the desired ASR mitigation.

3.2.2. *X-ray diffraction analysis*

To investigate the effect of the incorporation of NaMt/ONaMts on the evolutions of crystalline phases, especially the ASR-related products, XRD was conducted on the powders collected from the mortar bars immersed in 1 N NaOH solutions after 60 days. As shown in Fig. 5a, anhydrate clinker (C_2S/C_3S), cement hydration products (i.e., CH, C-S-H phases, AFt, etc.), calcite from the unavoidable carbonation, quartz from the reactive aggregates, and the well-defined ASR phases can be identified from the XRD patterns. In this study, the Na-K-Ca silicate hydrate minerals that are normally considered as the natural counterparts to ASR products, including cryptophyllite ($(K,Na)_4Ca_2Si_8O_{20}{\cdot}10H_2O$) (Zhang et al., 2017), rhodesite ($KCa_2Si_8O_{18.5}{\cdot}6.5H_2O$) (Katayama, 2012), okenite ($CaSi_2O_5{\cdot}2H_2O$) (Cole and Lancucki, 1983), kanemite ($NaHSi_2O_5{\cdot}3(H_2O)$) (Kirkpatrick et al., 2005), and makatite ($Na_2Si_4O_8(OH)_2{\cdot}4(H_2O)$) (Guthrie and Carey, 2015), were selected for peak fitting and quantifications. Due to the presence of sand in the mortars, quartz dominated the diffractogram, which is consistent with the observation by Shi et al. (Shi et al., 2018). Despite this, other characteristic peaks can still be identified for the Rietveld refinement, in which seven categories, such as quartz, anhydrates, amorphous, CH, crystalline ASR (the combined minerals discussed above), crystalline C-S-H, and others, were analyzed. Clinotobermorite, suolunite, tobermorite, foshagite, and rosenhahnite were considered as the crystalline C-S-H (Richardson, 2014), while calcite, xanthophyllite, ettringite, hydrotalcite, and gypsum are defined as others in the current study.

In accordance with TGA results, lower CH contents were obtained

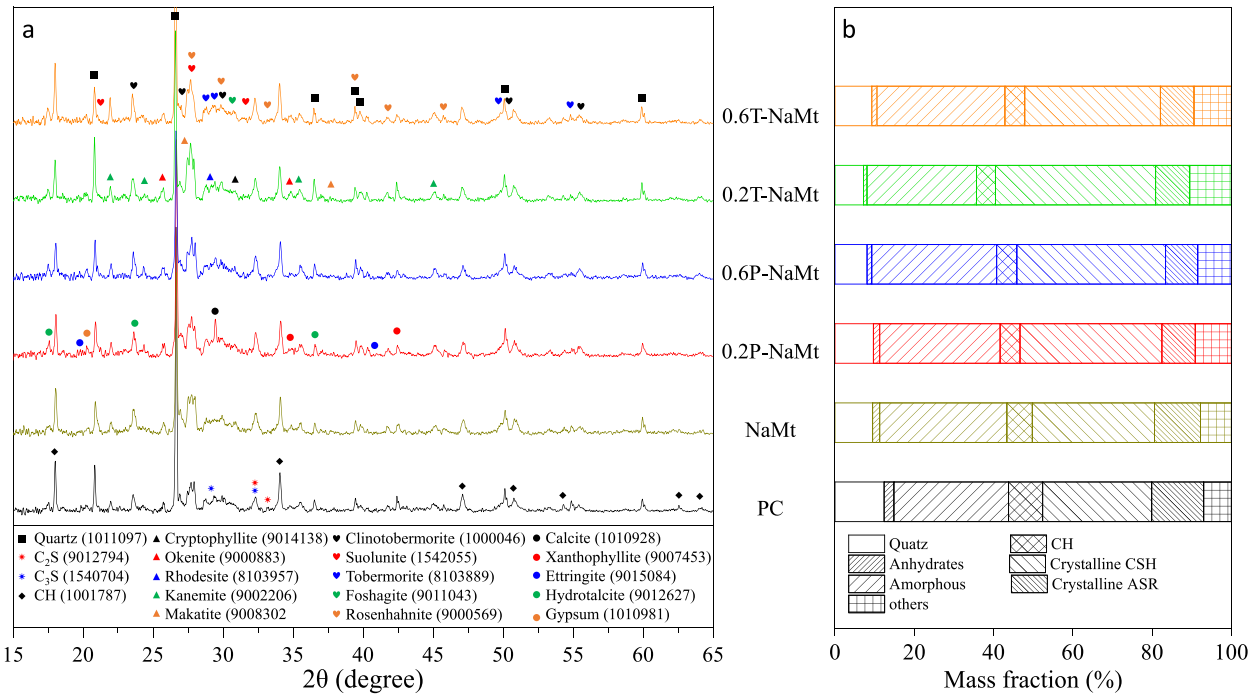

Fig. 5. (a) XRD patterns and (b) phase contents quantified by Rietveld refinement.

from the groups containing NaMt and ONaMts. PC showed a value of 8.6%, which decreased to 6.4% in NaMt, and then further reduced to 4.8–5.1% in the presence of ONaMts. Among all the groups, 0.2T-NaMt showed the lowest value of 4.8%. As discussed in Section 3.2.1, the less CH remaining in the ONaMt groups than NaMt might be mainly due to the enhanced pozzolanic reactivity by the organic functionalization. It is anticipated that the less available calcium is favorable to mitigate the formation of ASR gels. This can be confirmed by the fewer crystalline ASR products detected from the NaMt/ONaMt groups. PC exhibited 13.1% of crystalline ASR products, which decreased to 11.6% in NaMt. Further decreased crystalline ASR products in a range of 8.1–8.6% were detected from the NaMt/ONaMt groups, which are 5.0–4.5% and 3.5–3.0% lower than that of PC and NaMt, respectively. Again, 0.2P-NaMt showed the lowest content of crystalline ASR product, which is in line with the most reduced CH content. On the contrary, increased crystalline C-S-H was obtained by replacing cement with NaMt and ONaMts. NaMt yielded around 30.8% of crystalline C-S-H, which was 3.3% higher than that of PC. 0.2T-NaMt showed the highest crystalline C-S-H among all these groups, showing a value of 40.4%, which was 12.9% and 9.6% higher than PC and NaMt, respectively. It is worth noting that, in addition to the pozzolanic reaction and the enhanced cement hydration induced by the incorporation of NaMt and ONaMts, the crystallization of C-S-H can also be promoted by the elevated temperature (Krakowiak et al., 2018; Yazıcı et al., 2013) and alkalis (Jawed and Skalny, 1978) in the long ASR test. The increased C-S-H content and the decreased CH and crystalline ASR products explain the suppressed ASR expansion in the presence of ONaMts.

3.2.3. *ATR-FTIR spectroscopy*

Fig. 6 shows the ATR-FTIR spectra of the mortars after 60 days. The presence of quartz was identified by the v_1 of SiO_4 at ~798 cm^{-1} (Oruji et al., 2019), while the bands at ~1430 cm^{-1} and ~ 778 cm^{-1} are

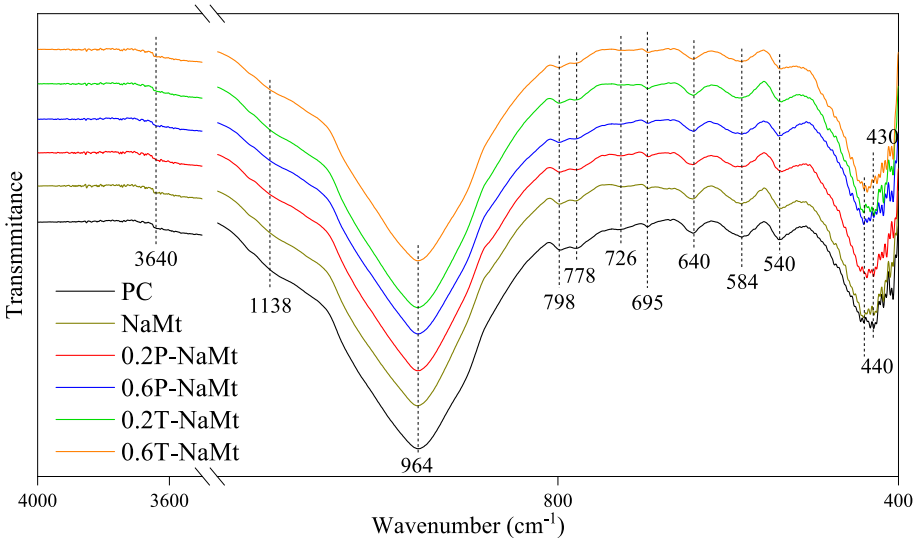

Fig. 6. ATR-FTIR spectra of the mortar samples after 60 days of treatment.

assigned to the stretching and out-of-plane bending vibrations of C—O bonds indicating the formation of carbonates during the test. The typical band at 3640 cm^{-1} is assigned to the O—H stretching vibration in CH. Due to the consumption of CH by both ASR and pozzolanic reaction in the groups with NaMt and ONaMts, this peak was not as significant as the one observed from the cement hydration system reported in the previous studies (Husillos-Rodríguez et al., 2022; Luo and Wei, 2022b), while PC still showed slightly higher intensity than the binary blends. The formation of the highly polymerized associations of Si—O stretching vibrations in the silicon-rich ASR gels can be indicated by the shoulder at around ~1138 cm^{-1} (Fernández-Jiménez et al., 2003). The peaks at ~695 cm^{-1}, ~640 cm^{-1}, ~584 cm^{-1}, and ~ 540 cm^{-1} are associated with the ASR gel's characteristic Si-O-Si deformation vibrations (Lodeiro et al., 2009; Shi et al., 2019). It can be observed that, compared with the control group (PC), these ASR-related peaks decreased due to the incorporation of NaMt and ONaMts. The lowest ASR-related peak intensities were found in 0.6P-NaMt and 0.6P-NaMt, indicating the highest efficiency in ASR mitigation in these two ONaMt groups, which is consistent with the volume expansion depression shown in Fig. 2.

The Q^2 sites of asymmetric stretching at ~964 cm^{-1} (Lodeiro et al., 2009) and bending vibrations at ~440 cm^{-1} (Yaseri et al., 2017) and ~ 430 cm^{-1} (El-Alfi and Gado, 2016) are assigned to C-S-H. Compared with PC, NaMt showed higher C-S-H-related bands indicating the enhanced cement hydration by the incorporation of NaMt. Again, as revealed by the further increased C-S-H bands, ONaMts exhibited higher efficiency than NaMt in enhancing cement hydration. The appearance of the symmetric stretching vibration of Al-O-Si at ~726 cm^{-1} (Panias et al., 2007) from the NaMt, especially the ONaMt groups, validating the formation of alumni-silicate hydrates due to the incorporation of NaMt/ONaMt.

3.2.4. *Raman spectroscopy*

Due to its excellent ability in characterizing amorphous materials, Raman spectroscopy has become an ideal technique for ASR gel investigation (Balachandran et al., 2017; Tang et al., 2021). In the current study, the Raman spectra focusing on three different spots (see Fig. 7a), i.e., the cement paste, the ASR gels formed in the aggregate cracks, and the ASR gels extruded to the cement paste, on the cross-section of selected mortar samples were collected and shown in Fig. 7b-7d, respectively. From Fig. 7b, the Q^2 sites at ~340 cm^{-1}, ~667 cm^{-1}, and 980 cm^{-1} presented in the silica chain structure of C-S-H dominate the spectra detected from the cement pastes, especially the ones incorporated with NaMt and ONaMts. However, a tremendous peak at ~1084 cm^{-1}, assigned to the Q^3 polymerization sites typically formed in ASR gels, was observed from PC. Due to the incorporation of NaMt or ONaMts, a substantial decrease was observed from this Q^3 peak, which is in line with the TGA, XRD, and ATR-FTIR results. In addition, the decreased CH due to pozzolanic reactions of NaMt clay particles was again observed from the evolution of the peak at ~1578 cm^{-1}, which is due to the stretching vibration of -OH in CH. No significant difference

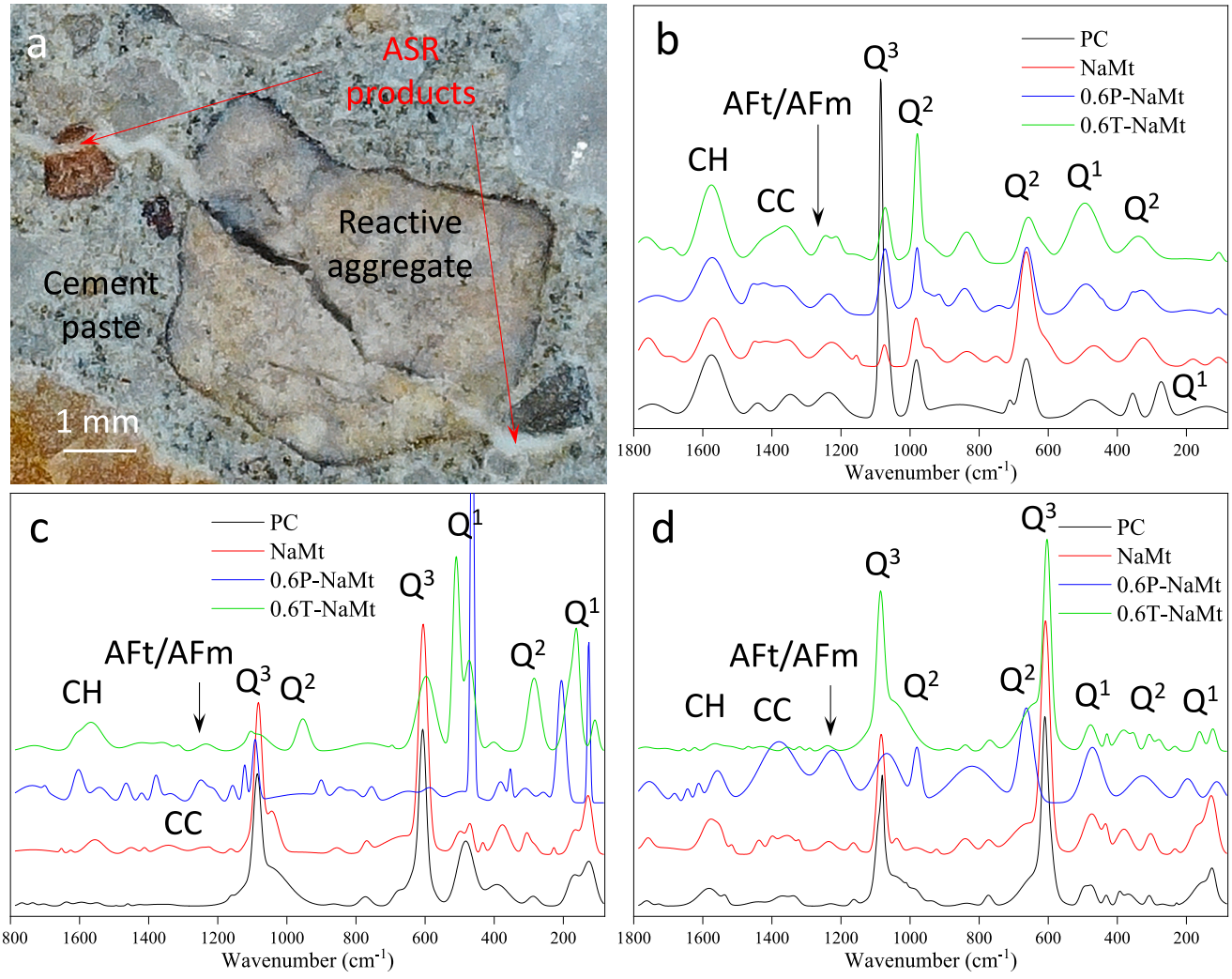

Fig. 7. (a) A cross-section of a mortar bar with a crack running through an aggregate filled with ASR gels, and Raman spectra of (b) cement paste, (c) ASR gels inside the aggregate crack, and (d) ASR gels extruded to the cement paste, after 60 days of immersion in 1 N NaOH at 80 °C.

was found from the sulfate phases (AFt/AFm) indicated by a peak at ~1235 cm^{-1} caused by the vibration of SO_4^{2-}.

From the ASR gels formed in aggregate cracks, the high intensity of the peaks between ~100 cm^{-1} and ~ 200 cm^{-1} and at 485 cm^{-1} corresponding to the Q^1 sites in quartz was detected from the area inside the aggregate cracks (see Fig. 7c), which might be due to the unreacted sand. In addition to the symmetrical stretching at ~1084 cm^{-1}, the symmetrical bending at ~607 cm^{-1} can also be assigned to the Q^3 sites, which confirmed the formation of ASR gels. The NaMt group showed comparable Q^3 peaks with PC, indicating the limited ASR mitigation efficiency of the raw NaMt. However, significant decreases in Q^3 peak intensity were observed from 0.6P-NaMt and 0.6T-NaMt, which indicates the suppressed formation of ASR gels and explain the mitigated ASR-induced expansion and cracking. Similar observations were found from the ASR gels extruded into the cement pastes as shown in Fig. 7d. The Q^3 peaks are relatively comparable in PC and NaMt, while it decreased dramatically in 0.6P-NaMt indicating the suppressed formation of ASR products. This explains the suppressed expansion and cracking of the mortars as Q^3 polymerization is considered the main reason for ASR gel's moisture update and swelling (Geng et al., 2020). However, in line with the expansion results, higher Q^3 peaks were observed from 0.6T-NaMt, which revealed the lower efficiency of TX100-modified NaMt in suppressing the formation of ASR products when compared with that functionalized with PONPE9. Furthermore, compared with PC and NaMt, higher Q^2 peaks were observed from 0.6P-NaMt and 0.6T-NaMt indicating the formation of additional C-S-H as a result of enhanced cement hydration and pozzolanic reactions in the presence of the functionalized ONaMts.

3.2.5. Microstructure investigation and element analysis

The microstructures of ASR gels formed in PC, 0.6T-NaMt, and 0.6P-NaMt are displayed in Figs. 8a to 8d. The characteristic layered structure of crystalline ASR gels, as well as the amorphous ASR gels that cover the crystalline one, were both observed in PC, which is similar to the previous studies (Leemann et al., 2016; Shi et al., 2020). From Fig. 8a and b, the crystalline ASR gels formed in PC showed an average thickness of around 80 nm and an average length of around 7.3 μm, while these two values become lower than 35 nm and 2.5 μm, respectively, in the selected ONaMts groups (see 0.6P-NaMt in Figs. 8c and 8d and 0.6T-NaMt in Fig. 8e and f). Furthermore, the crystalline ASR gels formed in both 0.6P-NaMt and 0.6T-NaMt exhibited a less-ordered structure compared to that observed in PC. A less amount of amorphous ASR gels in the surface and edge of the crystalline ASR gel sheets was also observed. It was reported (Gavrilenko et al., 2007; Kawamura and Iwahori, 2004) that the amorphous ASR gels are the primarily formed phases due to the fast dissolution of silica from highly reactive aggregate under the accelerated test conditions, and then the amorphous ASR gels crystallize with time. The coexistence of the amorphous and crystalline ASR gels indicates the high degree of ASR in PC. The incorporation of ONaMts into the mortars resulted in the formation of smaller crystalline ASR sheets and less amorphous ASR gels.

Figs. 9a to 9f present the EDS analyses of the crystalline and amorphous ASR gels formed in PC, 0.6P-NaMt, and 0.6T-NaMt, from which the average atomic ratios between calcium and silicon (Ca/Si), alkalis and silicon ([K + Na]/Si), and aluminum and silicon (Al/Si). The average Ca/Si vs. [K + Na]/Si and Ca/Si vs. Al/Ca are presented in Fig. 9g and h, respectively. The crystalline ASR gels formed in PC showed average Ca/Si and [K + Na]/Si atomic ratios of 0.25 and 0.39, respectively. Compared with C-S-H, the lower Ca/Si and higher [K + Na]/Si in ASR gels induce their high moisture absorption and swelling potential. Compared with the crystalline ASR products, a slightly higher Ca/Si of 0.26 was observed from the amorphous ASR gels, but the [K + Na]/Si was also increased to 0.44. Due to the incorporation of 0.6P-NaMt, both the crystalline and amorphous ASR gels showed decreased Ca/Si and [K + Na]/Si atomic ratios. The amorphous ASR gels formed in 0.6P-NaMt showed a Ca/Si of 0.21 and a [K + Na]/Si of 0.41, which are 19.2% and 6.8% lower than that in PC respectively. The same phenomenon was also observed from 0.6T-NaMt, which showed Ca/Si of 0.20 and 0.14 and [K + Na]/Si of 0.41 and 0.36 in its crystalline and amorphous ASR gels, respectively. From Fig. 19 g, an overall positive correlation between the Ca/Si and the [K + Na]/Si of ASR gels was observed. Both calcium and alkalis play critical roles in determining the properties of ASR gels. It was found that the formation of ASR gels first increased with the amount of calcium up to a Ca/Si ratio of 0.3 and then decreased at higher Ca/Si atomic ratios (Shi and Lothenbach, 2019). Sufficient amounts of alkalis (K and Na) are requisite for ASR gels, and an increase in [K + Na]/Si up to 1.0 can result in the formation of more ASR gels (Shi and Lothenbach, 2020). The swelling potential of ASR gels was found to decrease with calcium content up to a Ca/Si of 0.23 and the highest swelling pressure was obtained from the ASR gels with Ca/Si between 0.3 and 0.4 (Gholizadeh-Vayghan and Rajabipour, 2017a, 2017b). In previous studies (Gholizadeh-Vayghan and Rajabipour, 2017a, 2017b; Shi and Lothenbach, 2019; Vayghan et al., 2016; Wei et al., 2022) positive correlations between the swelling, water absorption and [K + Na]/Si of the ASR gels were reported, which are in line with the findings in this study. Therefore, in addition to the consumption of CH and the suppressed formation of Q^3 polymerization sites, the incorporation of ONaMts also decreased alkali contents in the ASR gels and made them less swellable.

In addition to the Ca/Si and [K + Na]/Si atomic ratios, the development of the Al/Ca ratio in the ASR gels was also determined. By comparing Fig. 9b, d, and f, the Al/Ca ratio of the ASR gels was found to increase in the presence of ONaMts. The Al/Ca ratios in the crystalline and amorphous ASR gels formed in PC are relatively comparable with values of 0.05 and 0.04, respectively. The limited aluminum detected in PC might be due to the aluminate from the cement (see Table 1). Due to the high amount of aluminate in NaMt, the Al/Ca ratios of the crystalline and amorphous ASR gels in 0.6P-NaMt were found to increase to 0.20 and 0.32, respectively. Similar changes were also observed from 0.6T-NaMt, in which the two values increased to 0.27 and 0.45, respectively. From Fig. 9h, a negative correlation between Al/Ca and Ca/Si of ASR gels was observed indicating the incorporation of aluminum into ASR gels induced by the incorporation of the functionalized ONaMts. The structure of the ASR gels can be changed by incorporating aluminum in four- and six-fold coordination (Krüger et al., 2023) to form a structure dominated by Q^2 sites instead of Q^3 sites (Leemann et al., 2015). Transformation of crystalline ASR gels to zeolite or its precursor (alkali alumino-silicate phase) was also documented (Hünger, 2007; Shi et al., 2018). This aluminum-induced structure change can result in a lower expansion potential in ASR gels (Luo et al., 2022; Shi and Lothenbach, 2022a), thereby suppressing their destructiveness to concrete.

3.2.6. Discussion of ASR mitigation mechanisms

The TGA and XRD quantifications of the current study indicate that the hydrtation of cement was enhanced in the presences of ONaMts, whereas CH was effectively consumed due to the pozzolanic reaction induced by the incorporation of ONaMts. This is due to the improvements of pozzolanic reactivity of NaMt after the non-ionic functionalization, which has been confirmed in the authors' previous study (Luo and Wei, 2022a). The free calcium from CH is considered the limiting factor in alkali recycling (Thomas, 2001), a dynamic process involving replacement of alkalis in the ASR products with calcium. In this way, CH serves as a buffer to maintain the alkalinity of the pore solution at a high level (Qiu et al., 2022), which keeps fueling the formation of additional ASR products. As a result, agreeing with the findings by (Lei et al., 2021), a positive correlation was observed between the ASR-induced expansion and CH content. Fig. 10a shows the relationship between the CH contents in the mortars quantified by TGA and XRD and the ASR-induced expansion obtained in this study. It can be seen that the ASR-induced expansion is positively correlated to the CH content in the matrix. In line with the precipitated CH contents, the ASR expansion is distributed in three distinct levels, where PC is the highest one and

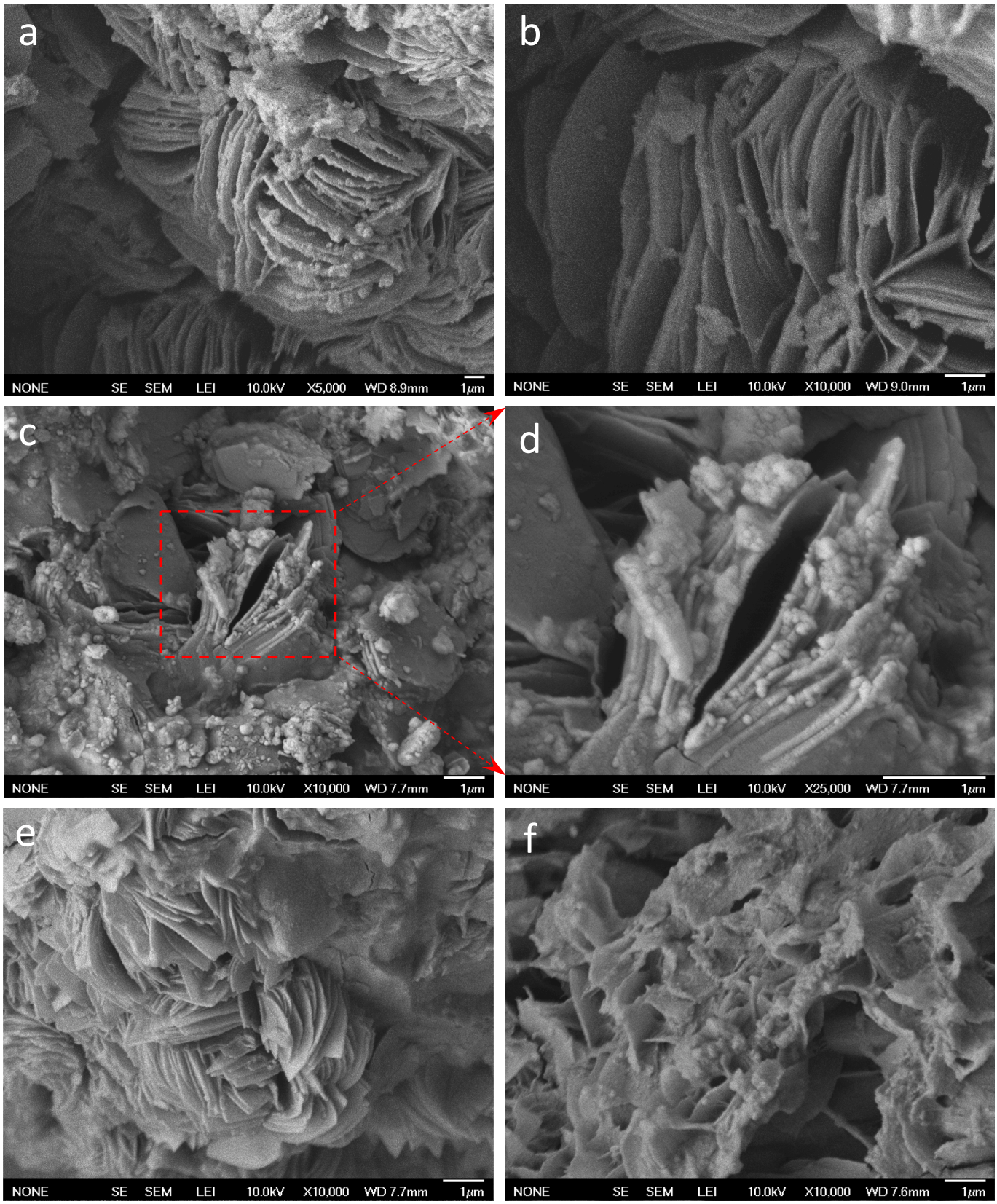

Fig. 8. Microstructures of the ASR gels formed in (a, b) PC, (c, d) 0.6P-NaMt, and (e, f) 0.6 T-NaMt.

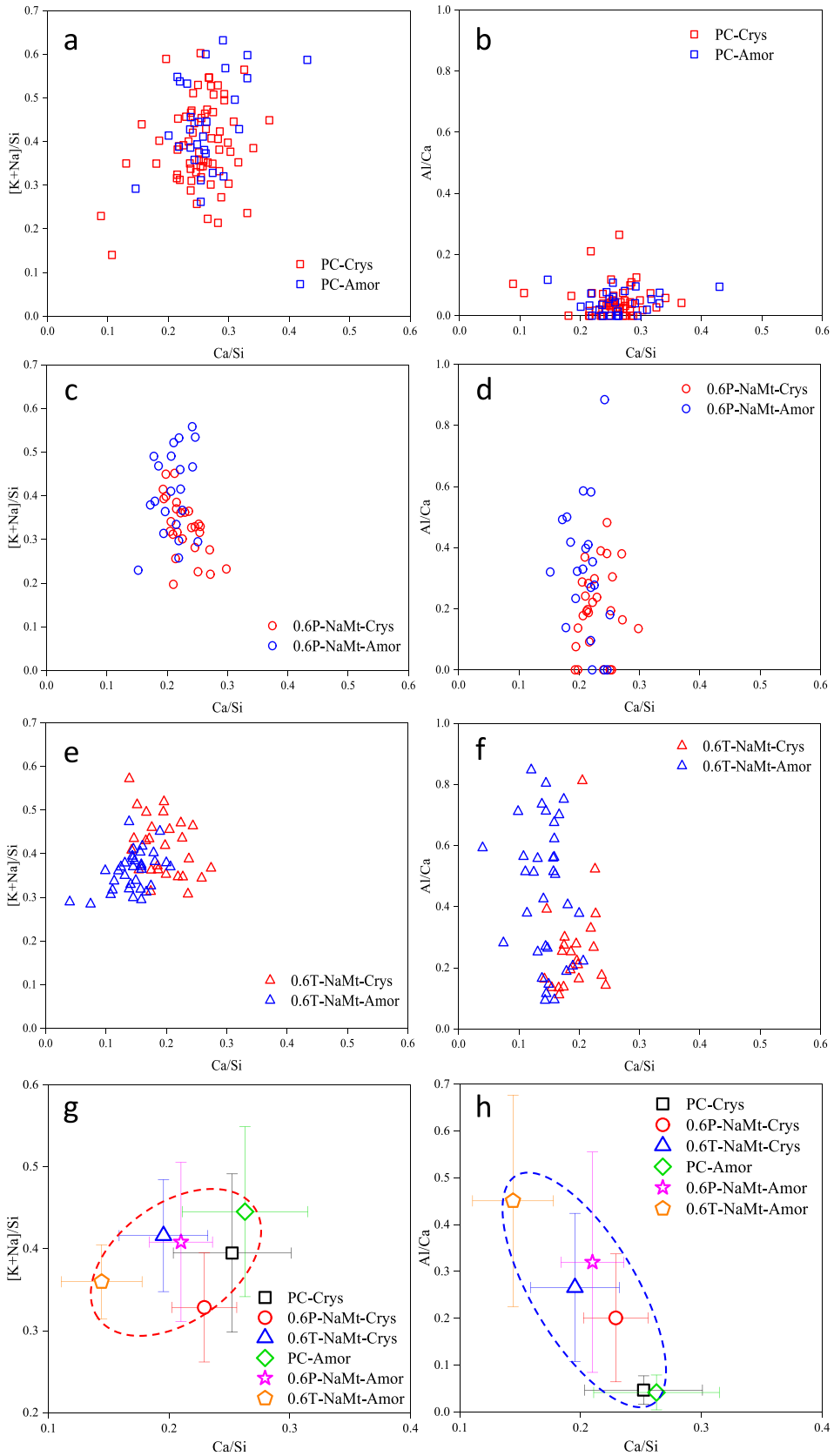

Fig. 9. Atomic ratios (a, c, e) [K + Na]/Si and (b, d, f) Al/Ca of the crystalline and amorphous ASR gels formed in (a, b) PC, (c, d) 0.6P-NaMt and (e, f) 0.6 T-NaMt as functions of their atomic ratios Ca/Si, (g) average [K + Na]/Si vs. average Ca/Si, and (h) average Al/Ca vs. Ca/Si of the ASR gels.

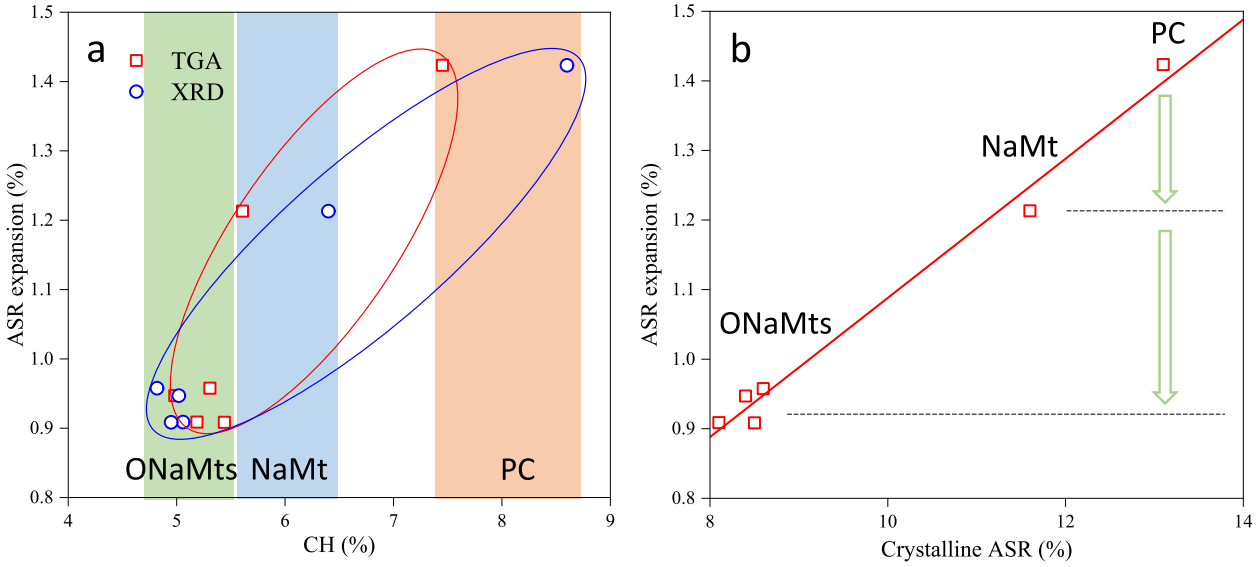

Fig. 10. Correlations between ASR-induced expansion and (a) CH content (determined by TGA and XRD) and (b) crystalline ASR content (determined by XRD).

ONaMts exhibit the most effective expansion suppression. In addition to CH content, a positive correlation between the amount of crystalline ASR gels quantified by XRD and the ASR-induced expansion was also observed (see Fig. 10b). Similarly, due to the different ASR mitigation efficiency, the crystalline ASR gels formed in the mortars showed three levels, where the formation of crystalline ASR gels was more significantly mitigated in the presence of ONaMts than raw NaMt.

The Al-rich nature of NaMt renders it a unique SCM in modifying the reaction products in both cement hydration and ASR. It has been observed in the authors' previous study that, after the non-ionic functionalization, the releases of Al and Si from NaMt in the cement pore solution can be impooved by 3.6 and 3.4 times, respectively (Luo and Wei, 2022a). The increased availability of Al and Si not only adjust the pH value of the system but also modify the elemental ratios and molecular structures of the reaction products. The FTIR and Raman results indicate the mitigated formation of Si—O stretching, Si-O-Si deformation, and Q^3 polymerization sites and the dominance of Q^2 sites in the ASR products, which agrees with the findings from (Leemann et al., 2015). The bridging Q^3 tetrahedron site of the sheet-like silicate structure is considered responsible for the moisture absorption in the interlayer spaces and volume swelling of ASR products (Kirkpatrick et al., 2005). The incorporation of Al in the ASR gels formed in the ONaMts groups was confirmed by the EDS analysis of this study. It has been well demonstrated that the incorporation of Al can result in decreased moisture absorption and suppressed expansion potential of ASR gels (Luo et al., 2022; Shi and Lothenbach, 2022b). The lower alkali-to-silica ratio and higher aluminum-to-calcium ratio detected from the ASR gels formed in mortars containing ONaMts provided an indication of the decreased expansion potential and destructiveness of the ASR gels. In addition, the decrease in the size of the layered crystalline ASR gels with less ordered structures and fewer amorphous ASR gels observed from the SEM images indicate the mitigated formation of ASR products in the presenceof ONaMts.

In addition to the chemical role of the functionalized ONaMts, it is anticipated that the particles size of ONaMts smaller than cement and the formation of additional C-S-H can result in a more densified microstructure over that of the plain cement matrix as demonstrated in the authors' previous studies (Luo and Wei, 2022b, 2023). The structure densification can suppress the diffusion of alkali ions (i.e., Na^+, K^+) and moisture in the cement matrix (Hay and Ostertag, 2021), therefeby mitigating the continouse formation of ASR products and their expansion.

It is worth noting that the ASR mitigation in the cement-ONaMt systems is a result of multiple chemical and physical mechanisms. The enhanced cement hydration and pozzolanic reactions in the presence of ONaMts, in particular the modified reaction products in the cement matrix, suppress the prerequisites of ASR and its continouse development. At a smaller scale, the formation of ASR gels and their molecular structures, as well as their hygroscopic expansion can be mitigated in the presence of ONaMts. Further investigations on the evolutions of physical and chemical properties of both amorphouse and crystalline ASR products at multiple length scales are needed to obtain a comprehensive understanding of the underlying mechanisms.

4. Conclusions

The enhanced efficiency of NaMt in ASR mitigation after functionalization with two non-ionic surfactants, PONPE9 and TX100, was validated in this study. The underlying mechanisms were uncovered by means of TGA, XRD, and ATR-FTIR spectroscopy of the mortar system, as well as in-situ characterization of ASR gels via Raman spectroscopy and SEM-EDS. The following main conclusions can be drawn:

1. Compared with raw NaMt, the incorporation of functionalized ONaMts exhibited a more effective role in suppressing the ASR-induced expansion. By incorporating 3 wt% 0.6P-NaMt and 0.6T-NaMt, the 14-day expansion was decreased by 0.36% and 0.33%, respectively. The highest expansion rate was decreased by up to 20.4%.
2. Agreeing well with the decreased ASR expansion, ONaMts presented an effective role in suppressing the cracking behavior of mortar outperforming the raw NaMt. This efficiency was found to increase with the dosages of both surfactants. The mortars containing 0.6PNaMt and 0.6TNaMt exhibited 70.4% and 63.6% lower average crack widths than that of PC, and 63.9% and 55.6% lower crack withs when compared with that containing raw NaMt.
3. From TGA and XRD results, less CH was precipitated in the mortars in the presence of ONaMts than NaMt, which might be due to the enhanced pozzolanic reactivity of NaMt after functionalization. The ASR-induced expansion is found to negatively correlate with the CH content but positively correlate with the content of crystalline ASR gels formed in the mortars.
4. Compared with raw NaMt, decreased Si—O stretching and Si-O-Si deformation vibrations and fewer Q^3 polymerization sites in ASR

gels were obtained from the ONaMt groups indicating the further suppressed formation of ASR products in the presence of functionalized ONaMt particles.
5. Due to the incorporation of ONaMts, the size of the layered crystalline ASR gels formed in the mortars decreased from 7.3 μm to 2.4 μm in length with less ordered structures and less amorphous ASR gels.
6. Lower alkali-to-silica ratio and higher aluminum-to-calcium ratio were detected from the ASR gels formed in mortars containing ONaMts, which provides an indication of the decreased expansion potential and destructiveness of the ASR gels.

CRediT authorship contribution statement

Dayou Luo: Investigation, Validation, Writing – original draft. **Jianqiang Wei:** Conceptualization, Methodology, Data curation, Supervision, Writing – review & editing, Funding acquisition.

Declaration of Competing Interest

The authors declare that they have no known competing financial interests or personal relationships that could have appeared to influence the work reported in this paper.

Data availability

Data will be made available on request.

Acknowledgment

This work was supported by the United States National Science Foundation (NSF) under award No. 1935799. The authors also acknowledge the support from the Transportation Infrastructure Durability Center at the University of Maine under grant 69A3551847101 (3.19) from the U.S. Department of Transportation's University Transportation Centers Program.

Appendix A. Particle size distribution of cement and NaMt/ONaMts

The particle size distributions of cement, NaMt, and ONaMts are shown in Fig. A1. It can be seen that the cement and NaMt possess median particle sizes of 12.2 μm and 15.7 μm, respectively. After ball milling, the 0.6T-NaMt and 0.6P-NaMt exhibited median particle sizes of 11.3 μm and 12.8 μm, respectively, which are comparable with that of the raw NaMt.

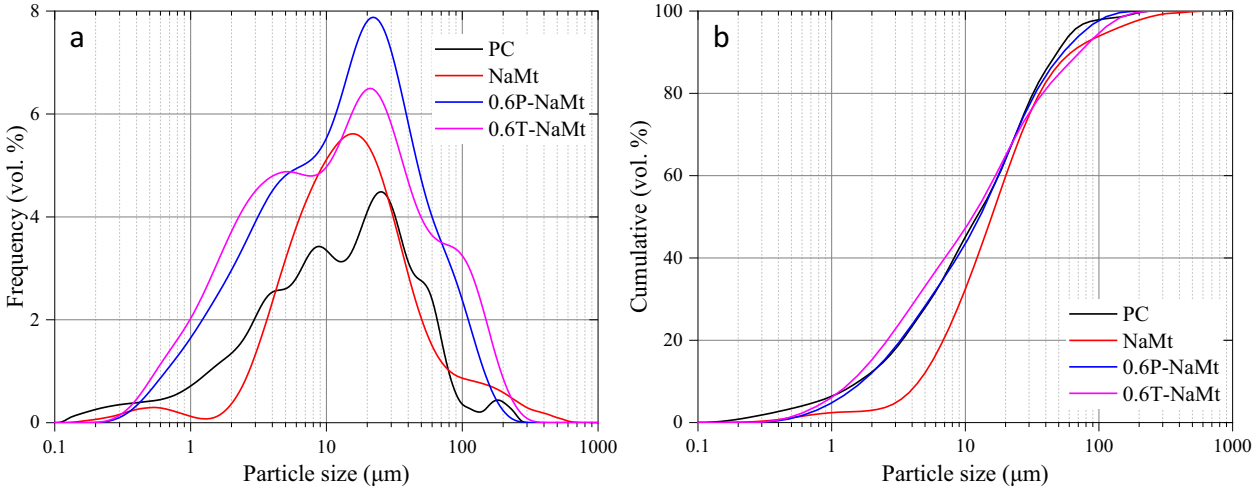

Fig. A1. Particle size distributions of the cement, NaMt, 0.6P-NaMt, and 0.6 T-NaMt: (a) the relative frequency of particles and (b) the volume of the particles smaller than a specific diameter.

References

ASTMC837, 2019. Standard Test Method for Methylene Blue Index of Clay. https://doi.org/10.1520/C0837-09R19.
ASTMC1260, 2022. Standard Test Method for Potential Alkali Reactivity of Aggregates (Mortar-Bar Method). https://doi.org/10.1520/C1260-22.
Balachandran, C., Muñoz, J., Arnold, T., 2017. Characterization of alkali silica reaction gels using Raman spectroscopy. Cem. Concr. Res. 92, 66–74. https://doi.org/10.1016/j.cemconres.2016.11.018.
Calabria-Holley, J., Papatzani, S., Naden, B., Mitchels, J., Paine, K., 2017. Tailored montmorillonite nanoparticles and their behaviour in the alkaline cement environment. Appl. Clay Sci. 143, 67–75. https://doi.org/10.1016/j.clay.2017.03.005.
Carles-Gibergues, A., Cyr, M., Moisson, M., Ringot, E., 2008. A simple way to mitigate alkali-silica reaction. Mater. Struct. 41, 73–83. https://doi.org/10.1617/s11527-006-9220-y.
Chang, T.-P., Shih, J.-Y., Yang, K.-M., Hsiao, T.-C., 2007. Material properties of Portland cement paste with nano-montmorillonite. J. Mater. Sci. 42, 7478–7487. https://doi.org/10.1007/s10853-006-1462-0.
Cole, W., Lancucki, C., 1983. Products formed in an aged concrete the occurrence of okenite. Cem. Concr. Res. 13, 611–618. https://doi.org/10.1016/0008-8846(83)90049-2.
Collins, C., Ideker, J.H., Willis, G., Kurtis, K., 2004. Examination of the effects of LiOH, LiCl, and LiNO3 on alkali–silica reaction. Cem. Concr. Res. 34, 1403–1415. https://doi.org/10.1016/j.cemconres.2004.01.011.
El-Alfi, E., Gado, R., 2016. Preparation of calcium sulfoaluminate-belite cement from marble sludge waste. Constr. Build. Mater. 113, 764–772. https://doi.org/10.1016/j.conbuildmat.2016.03.103.
Fernández-Jiménez, A., Puertas, F., Sobrados, I., Sanz, J., 2003. Structure of calcium silicate hydrates formed in alkaline-activated slag: influence of the type of alkaline activator. J. Am. Ceram. Soc. 86, 1389–1394. https://doi.org/10.1111/j.1151-2916.2003.tb03481.x.
Fournier, B., Ideker, J.H., Folliard, K.J., Thomas, M.D., Nkinamubanzi, P.-C., Chevrier, R., 2009. Effect of environmental conditions on expansion in concrete due to alkali–silica reaction (ASR). Mater. Charact. 60, 669–679. https://doi.org/10.1016/j.matchar.2008.12.018.
Gavrilenko, E., García del Amo, D., Calvo Pérez, B., García García, E., 2007. Comparison of ASR-gels in concretes against accelerated mortar bar test samples. Mag. Concr. Res. 59, 483–494. https://doi.org/10.1680/macr.2007.59.7.483.
Geng, G., Shi, Z., Leemann, A., Borca, C., Huthwelker, T., Glazyrin, K., Pekov, I.V., Churakov, S., Lothenbach, B., Dähn, R., 2020. Atomistic structure of alkali-silica reaction products refined from X-ray diffraction and micro X-ray absorption data. Cem. Concr. Res. 129 https://doi.org/10.1016/j.cemconres.2019.105958, 105958.

Gholizadeh-Vayghan, A., Rajabipour, F., 2017a. Quantifying the swelling properties of alkali-silica reaction (ASR) gels as a function of their composition. J. Am. Ceram. Soc. 100, 3801–3818. https://doi.org/10.1111/jace.14893.
Gholizadeh-Vayghan, A., Rajabipour, F., 2017b. The influence of alkali–silica reaction (ASR) gel composition on its hydrophilic properties and free swelling in contact with water vapor. Cem. Concr. Res. 94, 49–58. https://doi.org/10.1016/j.cemconres.2017.01.006.
Gražulis, S., Chateigner, D., Downs, R.T., Yokochi, A., Quirós, M., Lutterotti, L., Manakova, E., Butkus, J., Moeck, P., Le Bail, A., 2009. Crystallography open database–an open-access collection of crystal structures. J. Appl. Crystallogr. 42, 726–729. https://doi.org/10.1107/S0021889809016690.
Guthrie, G.D., Carey, J.W., 2015. A thermodynamic and kinetic model for paste–aggregate interactions and the alkali–silica reaction. Cem. Concr. Res. 76, 107–120. https://doi.org/10.1016/j.cemconres.2015.05.004.
Hay, R., Ostertag, C.P., 2021. New insights into the role of fly ash in mitigating alkali-silica reaction (ASR) in concrete. Cem. Concr. Res. 144, 106440. https://doi.org/10.1016/j.cemconres.2021.106440.
Hünger, K.-J., 2007. The contribution of quartz and the role of aluminum for understanding the AAR with greywacke. Cem. Concr. Res. 37, 1193–1205. https://doi.org/10.1016/j.cemconres.2007.05.009.
Husillos-Rodríguez, N., Martínez-Ramírez, S., Zarzuela, R., Mosquera, M., Blanco-Varela, M., Garcia-Lodeiro, I., 2022. Effect of alkoxysilane on early age hydration in Portland cement pastes. J. Build. Eng. 50 https://doi.org/10.1016/j.jobe.2022.104127, 104127.
Jawed, I., Skalny, J., 1978. Alkalies in cement: a review: II. Effects of alkalies on hydration and performance of Portland cement. Cem. Concr. Res. 8, 37–51. https://doi.org/10.1016/0008-8846(78)90056-X.
Kaladharan, G., Gholizadeh-Vayghan, A., Rajabipour, F., 2019. Review, sampling, and evaluation of landfilled fly ash. ACI Mater. J. 116, 113–122. https://doi.org/10.14359/51716750.
Katayama, T., 2012. ASR gels and their crystalline phases in concrete—Universal products in alkali–silica, alkali–silicate and alkali–carbonate reactions, Proc. In: 14th Int. Conf. Alkali Aggreg. React.(ICAAR), Austin, Texas, pp. 20–25.
Kawamura, M., Iwahori, K., 2004. ASR gel composition and expansive pressure in mortars under restraint. Cem. Concr. Compos. 26, 47–56. https://doi.org/10.1016/S0958-9465(02)00135-X.
Kim, T., Olek, J., 2012. Effects of sample preparation and interpretation of thermogravimetric curves on calcium hydroxide in hydrated pastes and mortars. Transp. Res. Rec. 2290, 10–18. https://doi.org/10.3141/2290-02.
Kim, T., Olek, J., Jeong, H., 2015. Alkali–silica reaction: kinetics of chemistry of pore solution and calcium hydroxide content in cementitious system. Cem. Concr. Res. 71, 36–45. https://doi.org/10.1016/j.cemconres.2015.01.017.
Kirkpatrick, R., Kalinichev, A., Hou, X., Struble, L., 2005. Experimental and molecular dynamics modeling studies of interlayer swelling: water incorporation in kanemite and ASR gel. Mater. Struct. 38, 449–458. https://doi.org/10.1617/14344.
Krakowiak, K.J., Thomas, J.J., James, S., Abuhaikal, M., Ulm, F.-J., 2018. Development of silica-enriched cement-based materials with improved aging resistance for application in high-temperature environments. Cem. Concr. Res. 105, 91–110. https://doi.org/10.1016/j.cemconres.2018.01.004.
Krüger, M.E., Heisig, A., Hilbig, H., Eickhoff, H., Heinz, D., Machner, A., 2023. Effect of aluminum on the structure of synthetic alkali-silica gels. Cem. Concr. Res. 166, 107088. https://doi.org/10.1016/j.cemconres.2022.107088.
Le Saoût, G., Kocaba, V., Scrivener, K., 2011. Application of the Rietveld method to the analysis of anhydrous cement. Cem. Concr. Res. 41, 133–148. https://doi.org/10.1016/j.cemconres.2010.10.003.
Leemann, A., Bernard, L., Alahrache, S., Winnefeld, F., 2015. ASR prevention—effect of aluminum and lithium ions on the reaction products. Cem. Concr. Res. 76, 192–201. https://doi.org/10.1016/j.cemconres.2015.06.002.
Leemann, A., Katayama, T., Fernandes, I., Broekmans, M.A., 2016. Types of alkali–aggregate reactions and the products formed. Constr. Mater. 169, 128–135. https://doi.org/10.1680/jcoma.15.00059.
Lei, J., Law, W.W., Yang, E.-H., 2021. Effect of calcium hydroxide on the alkali-silica reaction of alkali-activated slag mortars activated by sodium hydroxide. Constr. Build. Mater. 272 https://doi.org/10.1016/j.conbuildmat.2020.121868, 121868.
Li, T., Chai, Z., Yang, Z., Xin, Z., Sun, H., Yan, K., 2023. Insights into the influence mechanism of different interlayer cations on the hydration activity of montmorillonite surface: a DFT calculation. Appl. Clay Sci. 239, 106965. https://doi.org/10.1016/j.clay.2023.106965.
Lodeiro, I.G., Macphee, D.E., Palomo, A., Fernández-Jiménez, A., 2009. Effect of alkalis on fresh C–S–H gels. FTIR analysis. Cem. Concr. Res. 39, 147–153. https://doi.org/10.1016/j.cemconres.2009.01.003.
Luo, D., Wei, J., 2022a. Upgrading sodium montmorillonite into a reactive internal curing agent for sustainable cement composites through non-ionic functionalization. Compos. Part B Eng. 242, 110076. https://doi.org/10.1016/j.compositesb.2022.110076.
Luo, D., Wei, J., 2022b. Hydration kinetics and phase evolution of Portland cement composites containing sodium-montmorillonite functionalized with a Non-Ionic surfactant. Constr. Build. Mater. 333 https://doi.org/10.1016/j.conbuildmat.2022.127386, 127386.
Luo, D., Wei, J., 2023. Understanding the role of a novel internal conditioning technique with functionalized montmorillonite in cement hydration kinetics. Constr. Build. Mater. 385 https://doi.org/10.1016/j.conbuildmat.2023.131223, 131223.
Luo, D., Sinha, A., Adhikari, M., Wei, J., 2022. Mitigating alkali-silica reaction through metakaolin-based internal conditioning: New insights into property evolution and mitigation mechanism. Cem. Concr. Res. 159, 106888. https://doi.org/10.1016/j.cemconres.2022.106888.
Mesboua, N., Benyounes, K., Benmounah, A., 2018. Study of the impact of bentonite on the physico-mechanical and flow properties of cement grout. Cogent Eng. 5, 1446252. https://doi.org/10.1080/23311916.2018.1446252.
Millard, M., Kurtis, K., 2008. Effects of lithium nitrate admixture on early-age cement hydration. Cem. Concr. Res. 38, 500–510. https://doi.org/10.1016/j.cemconres.2007.11.009.
Morandeau, A., Thiery, M., Dangla, P., 2014. Investigation of the carbonation mechanism of CH and CSH in terms of kinetics, microstructure changes and moisture properties. Cem. Concr. Res. 56, 153–170. https://doi.org/10.1016/j.cemconres.2013.11.015.
Morris, A.L., MacArthur, M.W., Hutchinson, E.G., Thornton, J.M., 1992. Stereochemical quality of protein structure coordinates. Proteins: Struct. Funct. Bioinf. 12, 345–364. https://doi.org/10.1002/prot.340120407.
Oey, T., La Plante, E.C., Falzone, G., Hsiao, Y.-H., Wada, A., Monfardini, L., Bauchy, M., Bullard, J.W., Sant, G., 2020. Calcium nitrate: a chemical admixture to inhibit aggregate dissolution and mitigate expansion caused by alkali-silica reaction. Cem. Concr. Compos. 103592 https://doi.org/10.1016/j.cemconcomp.2020.103592.
Oruji, S., Brake, N.A., Guduru, R.K., Nalluri, L., Günaydın-Şen, Ö., Kharel, K., Rabbanifar, S., Hosseini, S., Ingram, E., 2019. Mitigation of ASR expansion in concrete using ultra-fine coal bottom ash. Constr. Build. Mater. 202, 814–824. https://doi.org/10.1016/j.conbuildmat.2019.01.013.
Panias, D., Giannopoulou, I.P., Perraki, T., 2007. Effect of synthesis parameters on the mechanical properties of fly ash-based geopolymers. Colloids Surf. A Physicochem. Eng. Asp. 301, 246–254. https://doi.org/10.1016/j.colsurfa.2006.12.064.
Papatzani, S., 2016. Effect of nanosilica and montmorillonite nanoclay particles on cement hydration and microstructure. Mater. Sci. Technol. 32, 138–153. https://doi.org/10.1179/1743284715Y.0000000067.
Qiu, X., Chen, J., Ye, G., De Schutter, G., 2022. A 3D reactive transport model for simulation of the chemical reaction process of ASR at microscale. Cem. Concr. Res. 151, 106640. https://doi.org/10.1016/j.cemconres.2021.106640.
Rajabipour, F., Giannini, E., Dunant, C., Ideker, J.H., Thomas, M.D., 2015. Alkali–silica reaction: current understanding of the reaction mechanisms and the knowledge gaps. Cem. Concr. Res. 76, 130–146. https://doi.org/10.1016/j.cemconres.2015.05.024.
Richardson, I.G., 2014. Model structures for C-(a)-S-H (I). Acta Crystallogr. Sect. B: Struct. Sci. Cryst. Eng. Mater. 70, 903–923. https://doi.org/10.1107/S2052520614021982.
Saha, A.K., Khan, M.N.N., Sarker, P.K., Shaikh, F.A., Pramanik, A., 2018. The ASR mechanism of reactive aggregates in concrete and its mitigation by fly ash: a critical review. Constr. Build. Mater. 171, 743–758. https://doi.org/10.1016/j.conbuildmat.2018.03.183.
Sanchez, L., Drimalas, T., Fournier, B., Mitchell, D., Bastien, J., 2018. Comprehensive damage assessment in concrete affected by different internal swelling reaction (ISR) mechanisms. Cem. Concr. Res. 107, 284–303. https://doi.org/10.1016/j.cemconres.2018.02.017.
Shi, Z., Lothenbach, B., 2019. The role of calcium on the formation of alkali-silica reaction products. Cem. Concr. Res. 126, 105898. https://doi.org/10.1016/j.cemconres.2019.105898.
Shi, Z., Lothenbach, B., 2020. The combined effect of potassium, sodium and calcium on the formation of alkali-silica reaction products. Cem. Concr. Res. 127, 105914. https://doi.org/10.1016/j.cemconres.2019.105914.
Shi, Z., Lothenbach, B., 2022a. Role of aluminum and lithium in mitigating alkali-silica reaction—a review. Front. Mater. 8, 596. https://doi.org/10.3389/fmats.2021.796396.
Shi, Z., Lothenbach, B., 2022b. Role of aluminum and lithium in mitigating alkali-silica reaction—a review. Front. Mater. 8 https://doi.org/10.3389/fmats.2021.796396, 796396.
Shi, Z., Shi, C., Zhang, J., Wan, S., Zhang, Z., Ou, Z., 2018. Alkali-silica reaction in waterglass-activated slag mortars incorporating fly ash and metakaolin. Cem. Concr. Res. 108, 10–19. https://doi.org/10.1016/j.cemconres.2018.03.002.
Shi, Z., Geng, G., Leemann, A., Lothenbach, B., 2019. Synthesis, characterization, and water uptake property of alkali-silica reaction products. Cem. Concr. Res. 121, 58–71. https://doi.org/10.1016/j.cemconres.2019.04.009.
Shi, Z., Park, S., Lothenbach, B., Leemann, A., 2020. Formation of shlykovite and ASR-P1 in concrete under accelerated alkali-silica reaction at 60 and 80 C. Cem. Concr. Res. 137, 106213. https://doi.org/10.1016/j.cemconres.2020.106213.
Taleb, K., Pillin, I., Grohens, Y., Saidi-Besbes, S., 2018. Gemini surfactant modified clays: effect of surfactant loading and spacer length. Appl. Clay Sci. 161, 48–56. https://doi.org/10.1016/j.clay.2018.03.015.
Tang, C., Ling, T.-C., Mo, K.H., 2021. Raman spectroscopy as a tool to understand the mechanism of concrete durability—a review. Constr. Build. Mater. 268 https://doi.org/10.1016/j.conbuildmat.2020.121079, 121079.
Thomas, M., 2001. The Role of Calcium Hydroxide in Alkali Recycling in Concrete, Materials Science of Concrete Special Volume on Calcium Hydroxide in Concrete. American Ceramic Society Westerville, OH, pp. 269–280.
Trottier, C., Ziapour, R., Zahedi, A., Sanchez, L., Locati, F., 2021. Microscopic characterization of alkali-silica reaction (ASR) affected recycled concrete mixtures induced by reactive coarse and fine aggregates. Cem. Concr. Res. 144, 106426. https://doi.org/10.1016/j.cemconres.2021.106426.
Trümer, A., Ludwig, H.-M., Schellhorn, M., Diedel, R., 2019. Effect of a calcined Westerwald bentonite as supplementary cementitious material on the long-term performance of concrete. Appl. Clay Sci. 168, 36–42. https://doi.org/10.1016/j.clay.2018.10.015.
Vayghan, A.G., Rajabipour, F., Rosenberger, J.L., 2016. Composition–rheology relationships in alkali–silica reaction gels and the impact on the gel's deleterious behavior. Cem. Concr. Res. 83, 45–56. https://doi.org/10.1016/j.cemconres.2016.01.011.

Wei, J., Gencturk, B., 2019. Hydration of ternary Portland cement blends containing metakaolin and sodium bentonite. Cem. Concr. Res. 123 https://doi.org/10.1016/j.cemconres.2019.05.017.

Wei, J., Gencturk, B., Jain, A., Hanifehzadeh, M., 2019. Mitigating alkali-silica reaction induced concrete degradation through cement substitution by metakaolin and bentonite. Appl. Clay Sci. 182, 105257. https://doi.org/10.1016/j.clay.2019.105257.

Wei, S., Zheng, K., Zhou, J., Prateek, G., Yuan, Q., 2022. The combined effect of alkalis and aluminum in pore solution on alkali-silica reaction. Cem. Concr. Res. 154, 106723. https://doi.org/10.1016/j.cemconres.2022.106723.

Wu, J., Liu, S., Deng, Y., Zhang, G., Zhan, L., 2022. Microscopic phase identification of cement-stabilized clay by nanoindentation and statistical analytics. Appl. Clay Sci. 224, 106531. https://doi.org/10.1016/j.clay.2022.106531.

Yaseri, S., Hajiaghaei, G., Mohammadi, F., Mahdikhani, M., Farokhzad, R., 2017. The role of synthesis parameters on the workability, setting and strength properties of binary binder based geopolymer paste. Constr. Build. Mater. 157, 534–545. https://doi.org/10.1016/j.conbuildmat.2017.09.102.

Yazıcı, H., Deniz, E., Baradan, B., 2013. The effect of autoclave pressure, temperature and duration time on mechanical properties of reactive powder concrete. Constr. Build. Mater. 42, 53–63. https://doi.org/10.1016/j.conbuildmat.2013.01.003.

Zhang, C., Sorelli, L., Fournier, B., Duchesne, J., Bastien, J., Chen, Z., 2017. Stress-relaxation of crystalline alkali-silica reaction products: Characterization by micro- and nanoindentation and simplified modeling. Constr. Build. Mater. 148, 455–464. https://doi.org/10.1016/j.conbuildmat.2017.05.069.